Hainzl, S. (2022): ETAS-Approach Accounting for Short-Term Incompleteness of Earthquake Catalogs. - Bulletin of the Seismological Society of America, 112, 494-507.

https://doi.org/10.1785/0120210146

ETAS-approach accounting for short-term incompleteness of earthquake catalogs

Sebastian Hainzl
GFZ German Research Centre for Geosciences, Potsdam, Germany

hainzl@gfz-potsdam.de

The author acknowledges there are no conflicts of interest recorded.

Abstract

The Epidemic-Type Aftershock Sequence (ETAS) model is a powerful statistical model to explain and forecast the spatiotemporal evolution of seismicity. However, its parameter estimation can be strongly biased by catalog deficiencies, particularly short-term incompleteness related to missing events in phases of high seismic activity. Recent studies have shown that these short-term fluctuations of the completeness magnitude can be explained by the blindness of detection algorithms after earthquakes, preventing the detection of events with a smaller magnitude. Based on this assumption, I derive a direct relation between the true and detectable seismicity rate and magnitude distributions, respectively. These relations only include one additional parameter, the so-called blind time T_b, and lead to a closed-form maximum likelihood formulation to estimate the ETAS parameters directly accounting for varying completeness. Tests using synthetic simulations show that the true parameters can be resolved from incomplete catalogs. Finally, I apply the new model to California's most prominent mainshock-aftershock sequences in the last decades. The results show that the model leads to superior fits with T_b decreasing with time, indicating improved detection algorithms. The estimated parameters significantly differ from the estimation with the standard approach, indicating higher b-values and larger trigger potentials than previously thought.

Introduction

The completeness magnitude M_c is defined as the magnitude of the smallest earthquakes, which the existing seismic network can detect everywhere. Its value depends on the quantity and configuration of the seismic stations and their signal-to-noise level. Significant M_c-variations are often related to network changes as the installation of new stations or failure of old ones. However, even in periods with constant network configuration, recording algorithm, and environment noise condition, the M_c-level can vary. In particular, M_c often increases during high seismic activity, such as the first days of aftershocks following mainshocks (Kagan, 2004) or intense swarm activity (Hainzl, 2016a). Such rate-dependent, short-term M_c-fluctuations can bias the estimations of essential seismicity parameters for seismic hazard assessment, such as the b-value of the frequency-magnitude distribution or the aftershock productivity (Kagan, 2004). Thus, it is important to consider the time-dependence of data completeness in applications of seismicity models.

The state-of-the-art model to fit and forecast seismicity in space and time is the so-called Epidemic-Type Aftershock Sequence (ETAS) model introduced by Ogata (1988; 1998). The ETAS model fits the earthquake rate as a linear superposition of a constant background rate $\mu(\vec{x})$ and decaying rates of ongoing aftershock sequences triggered by past events. It is described by

$$R_0(t,\vec{x}) = \mu(\vec{x}) + \sum_{i:t_i<t} K\,10^{\alpha(m_i - M_{\min})}\,(c+t-t_i)^{-p}\;\xi(\vec{x}-\vec{x}_i, m_i)\ , \tag{1}$$

where the index i refers to events occurred in the past at times t_i with epicenters $\vec{x}_i$ and magnitudes $m_i \geq M_{min} \geq M_c$. In general, the ETAS model is estimated for $M_{min} = M_c$, but sometimes a higher cutoff magnitude M_{min} may be useful to reduce the computational load. The spatial probability density function ξ for the triggered aftershocks is not well-constrained but typically assumed to be power-law-type. The temporal decay function and the productivity-scaling are better constrained: The time function matches the well-known Omori-Utsu law and the total aftershock number scales exponentially with magnitude of the trigger event; in agreement with observations (Utsu et al., 1995; Hainzl and Marsan, 2008). The ETAS-estimation of the scaling parameter α, which determines the increase of the direct aftershock number with mainshock magnitude, is typically significantly less than the b-value (Hainzl and Marsan, 2008). However, this apparent result might be biased by the short-time incompleteness of earthquake catalogs. Furthermore, the estimated c-value is likely affected by missing events as also indicated by Hainzl (2016b).

It has been already recognized that short-term incompleteness potentially biases the ETAS-estimations (Hainzl et al., 2013; Omi et al., 2013; Zhuang et al., 2017). Therefore, several approaches have been introduced to deal with this issue. For example, Hainzl et al. (2013) excluded the likely incomplete intervals from the fitting period of the ETAS model to the observed seismicity. For this purpose, they used an empirical relationship for California that relates the incompleteness period to the mainshock magnitude and the basic completeness level M_c (Helmstetter et al., 2006). However, in this approach, a significant amount of data is neglected, which weakens the model constraint. Furthermore, the results might still be affected by incompleteness during intensive swarm activity not related to a large mainshock. Alternatively, a replenishment algorithm has been introduced by Zhuang et al. (2017), which adds artificial events in the magnitude range identified to be incompletely recorded. While this method can compensate for missing events, it requires a manual definition of the time-evolution of the incompleteness magnitude. Furthermore, Omi et al. (2013; 2014) directly considered the time-varying completeness within the model fit. In this case, the ETAS model for early aftershocks is fitted, assuming an error function as detection probability for earthquake magnitudes with a mean value shifting in time. While this approach is promising, it requires estimating the time-dependence of the detection function from sparse data.

In this paper, a closed-form of the ETAS model is introduced (Section *Theory*), which consistently accounts for rate-dependent incompleteness adding only one additional fitting parameter, the blind time T_b. The modified ETAS model accounts for the detection's probability dependence on the event's magnitude and actual earthquake rate. This probability results from the simple assumption that an earthquake cannot be detected if it occurs within T_b after an event of larger magnitude (Hainzl, 2016a,b; de Arcangelis et al., 2018). The modification allows estimating, using a maximum likelihood approach, simultaneously the true

ETAS-parameters and b-value from earthquake catalogs with time-dependent completeness. For demonstration, the model is tested for synthetic sequences and applied to California's most prominent mainshock-aftershock sequences in the last decades (Section *Applications*).

Theory

In the following, M_c refers to the basic completeness magnitude of the catalog defining the completeness level in times of low seismicity. Furthermore, following the nomenclature of de Arcangelis et al. (2018), the modified ETAS model accounting for catalog incompleteness, which results from a blind time of detection algorithms after an earthquake occurrence, is called ETASI. For a closed formulation of this model, the relevant results of Hainzl (2016a; 2016b) are firstly summarized in the first subsection before the ETASI model with its maximum likelihood estimation is formulated in second subsection.

Rate-dependent incompleteness

The approach is based on the simple assumption that an earthquake of magnitude m cannot be properly distinguished and thus becomes not detectable by the seismogram analysis if it occurs less than a blind time T_b after an event of equal or larger magnitude (Hainzl, 2016a; Lippiello et al., 2016). Based on this, Hainzl (2016b) derived the functional form of the apparent seismicity rate R and magnitude distribution F for the recorded, incomplete catalog data. In particular, R and F depend on the true underlying rate R_0 at time t and the time-invariant, true magnitude distribution F_0.

The probability to observe an earthquake with a specific magnitude $m \geq M_c$ at time t is given by the probability that no earthquake occurred between time $t - T_b$ and t with a magnitude larger than m. Assuming an (inhomogeneous) Poisson process with the true rate R_0, this detection probability p_d is given by

$$p_d(m, t) = \exp[-N_0(t)\, F_0(m)] \ , \tag{2}$$

where $\mathrm{F}_0(m)$ is the true complementary cumulative distribution function of the earthquake magnitudes and N_0 is the true number of expected $m \geq M_c$ events, i.e. the integral of $R_0(t)$, in the time interval $[t - T_b, t]$. Note that the product $N_0(t)\, F_0(m)$ is simply the expected number of events with magnitude larger than m occuring in the interval T_b.

With this detection probability, both the apparent rate and magnitude distribution can be analytically determined. Hainzl (2016b) showed that, specifically, the apparent rate is given by

$$R(t) = \frac{R_0(t)}{N_0(t)} \left(1 - e^{-N_0(t)}\right) \approx \frac{1}{T_b} \left(1 - e^{-T_b\, R_0(t)}\right) \ , \tag{3}$$

and the apparent magnitude distribution becomes

$$F(m,t) = \frac{1 - e^{-N_0(t)\,F_0(m)}}{1 - e^{-N_0(t)}} \approx \frac{1 - e^{-R_0(t)\,T_b\ F_0(m)}}{1 - e^{-R_0(t)T_b}} \ . \tag{4}$$

In both equations, the approximation is assumed to hold because the seismicity rates are usually not significantly varying over the time scale of T_b, which is in the order of seconds to minutes; thus $N_0(t) \approx R_0(t)T_b$.

Figure 1 illustrates these relations for different R_0 and T_b values. Panel (a) shows the deviation of the apparent rate from the true one and the convergence of R to its maximum value $1/T_b$ for increasing R_0-values. The frequency-magnitude distribution of the detected events is shown in panel (b), assuming the Gutenberg-Richter (GR) law for the frequency-magnitude distribution

$$F_0(m) = 10^{-b(m-M_c)} \tag{5}$$

with $b = 1$. It becomes obvious that the effect of incompleteness strongly increases with increasing R_0 and T_b in both cases.

ETAS model for rate-dependent incompleteness (ETASI)

For the ETAS model, the functional forms of R and F can be specified. In the following, we refer for simplicity to the time-dependent ETAS model

$$R_0(t) = \mu + \sum_{i:t_i<t} K\,10^{\alpha(m_i-M_c)}\,(c+t-t_i)^{-p} \quad , \tag{6}$$

which is related to the integration of Eq. (1) over the region of interest and setting $M_{\min} = M_c$. This choice firstly helps to simplify the presentation and secondly avoids the complication of modeling the spatial distribution. Due to lacking information, the spatial aftershock triggering is usually assumed to be isotropic, although real distributions are anisotropic due to the rupture extension, slip variability, and heterogeneous crustal properties, respectively. The assumption of isotropy is known to significantly bias the parameter estimations; specifically, the α-value (Hainzl et al., 2008; Seif et al., 2017). However, this paper focuses on clarifying the effect of considering short-term incompleteness in the ETAS approach. Thus the time-dependent model is more appropriate. In any case, it is straightforward to extend the same concept to the spatiotemporal ETAS model (Eq. 1), as discussed in Section *Discussion*.

Furthermore, we consider the Gutenberg-Richter (GR) law for the frequency-magnitude distribution (Eq. 5) with its probability density function

$$f_0(m) = \ln(10)\,b\,10^{-b(m-M_c)} \ . \tag{7}$$

In the standard approach, the ETAS-model rate $R_0(t)$ and the GR distribution are directly fitted to the recorded earthquakes by maximizing the likelihood function. For N observed earthquakes occurred at times $t_i \in [T_1, T_2]$ with magnitudes $m_i \geq M_c$ ($i = 1 \ldots N$), the log-likelihood ($\mathcal{LL}_0$) function is then given by:

$$\begin{aligned}
\mathcal{LL}_0 &= \sum_{i=1}^{N} \ln\left[R_0(t_i) f_0(m_i)\right] - \int_{T_1}^{T_2} R_0(t)\; dt \\
&= \sum_{i=1}^{N} \ln\left[f_0(m_i)\right] + \left[\sum_{i=1}^{N} \ln\left[R_0(t_i)\right] - \int_{T_1}^{T_2} R_0(t)\; dt\right] \\
&= \mathcal{LL}_{GR} + \mathcal{LL}_{ETAS} \qquad (8)
\end{aligned}$$

In this case, the optimization of the ETAS-parameters and that of the b-value can be separated. The maximization of $\mathcal{LL}_{GR} = \sum_{i=1}^{N} \ln[f_0(m_i)] = N \ln\left[\ln(10)b\right] - \ln(10)b \sum_{i=1}^{N}(m_i - M_c)$ leads to the analytic Aki-estimator

$$b = \frac{\log(e)}{\bar{m} - M_c} \qquad (9)$$

with the mean magnitude $\bar{m}$ (Aki, 1965). The optimization of $\mathcal{LL}_{ETAS}$ has to be done numerically.

However, the maximization of Eq. (8) is biased by the short-term incompleteness of recorded catalogs. Thus, the ETAS parameters resulting from optimizing $\mathcal{LL}_0$ do not necessarily represent the underlying physical process. The resulting parameters are optimized to describe the incomplete data set's evolution; in particular, they fit the numerous small magnitude events that are most affected by the incompleteness. Furthermore, the validity of the Gutenberg-Richter law is assumed to hold for the recorded earthquakes at all times. However, this assumption is not valid, as, e.g., demonstrated in detail by Marsan & Ross (2021) for the 1999 M7.1 Ridgecrest sequence. The mean magnitude is significantly higher at short times after mainshocks due to missing events. However, such biased estimations due to short-term incompleteness can be avoided by applying the same maximum likelihood approach to fit the incomplete, observational data but replacing the true functions (R_0, F_0) by the apparent rate and magnitude functions (R, F) accounting for this incompleteness.

Taking into account the functional dependence of the apparent rate $R(t)$ and the apparent frequency-magnitude distribution on the true functions $R_0(t)$ and $F_0(m)$ (Eqs. 3 & 4), the maximum likelihood fit of the apparent functions to the observed data can be used to estimate the true parameters of the ETAS and GR model. In particular, the $\mathcal{LL}$-value is in this case given by

$$\mathcal{LL} = \sum_{i=1}^{N} \ln\left[R(t_i) f(m_i, t_i)\right] - \int_{T_1}^{T_2} R(t)\, dt$$

$$= \sum_{i=1}^{N} \ln\left[f(m_i, t_i)\right] + \sum_{i=1}^{N} \ln\left[R(t_i)\right] - \int_{T_1}^{T_2} R(t)\, dt \qquad (10)$$

where $R(t)$ is given by Eq. (3) in combination with Eq. (6). The probability density function $f(m, t)$, which describes the magnitude distribution of the incompletely recorded events, is equal to the negative derivative of the complementary cumulative distribution function F provided in Eq. (4) using the true GR distribution F_0 given in Eq. (5). Specifically, the apparent probability density function of the magnitudes is given by

$$f(m, t) = \ln(10) b\, N_0(t) \frac{10^{-b(m-M_c)}\, e^{-N_0(t)\, 10^{-b(m-M_c)}}}{1 - e^{-N_0(t)}} . \qquad (11)$$

In this case, the optimization of the b-value and the ETAS parameters cannot be separated. The reason is that f depends not only on the magnitude but also on N_0 and consequently on the ETAS parameters. In addition to the standard parameters $(b, \mu, K, \alpha, c, p)$, the $\mathcal{LL}$-value depends on the blind time T_b. Therefore, the maximum likelihood search involves seven instead of six free parameters.

Applications

The ETASI model is first applied to synthetic sequences to test the ability to retrieve the known true parameters from incomplete earthquake catalogs. Then, the same approach is applied to selected mainshock-aftershock sequences in California.

Synthetic simulations

The analyzed synthetic sequences were simulated with the ETAS model using the inverse transform method (Felzer et al., 2002; Zhuang and Touati, 2015) with fixed parameters $\mu = 1.0$ d^{-1}, $K = 0.0035$, $\alpha = 1.0$, $c = 0.001$ d, $p = 1.2$, $b = 1.0$, $M_{min} = 2.0$, and $M_{max} = 7.0$. These values correspond to a theoretical branching ratio of 0.8, meaning that 80% of the events are aftershocks on average (Helmstetter & Sornette, 2002). Each simulation lasts for 100 days, with an M6 mainshock occurring approximately after ten days. Specifically, the times of the background events were first randomly selected, assuming a stationary Poisson process with the rate μ, and then the magnitude of the background event that occurred closest to 10 days was set to 6. In contrast, all other events' magnitudes were randomly selected from the Gutenberg-Richter distribution between 2 and 7, assuming $b = 1$. In this way, each simulation consists of a significant number of aftershocks well centered in the simulated time interval. For each sequence, all non-detectable earthquakes occurring less than a blind time of $T_b = 60$ s after a larger magnitude event were removed to create an analogon to real incomplete catalogs.

A magnitude versus time plot of such a simulated sequence is shown in Fig. 2(a). The original ETAS simulation comprises all data points, but each of the events marked by crosses occurs within $T_b = 60$ s after an event with a larger magnitude and is not included in the analyzed (recorded) catalog (points). The incomplete catalog consists of 921 events, which is 60% of the original catalog. The inset shows the same data as a function of the time relative to the M6 event on a logarithmic scale. In this semi-logarithmic representation, the data gap (crosses) directly after the mainshock is visible for small magnitudes. For comparison, the dashed line shows the empirical completeness function for mainshocks derived for mainshocks in California (Helmstetter et al., 2006)

$$M_c(M, t) = M - 4.5 - 0.75 \log(t) \ , \qquad (12)$$

where the mainshock's magnitude M is 6.0 in our case. The empirical curve is found to well approximate the time-dependence of the completeness magnitude of the first period after the mainshock but does not account for missing events after larger aftershocks in the beginning and the remainder of the sequence. However, single events are also missed in periods without large events, e.g., the earthquake with magnitude 2.02 at day 33, which occurred shortly after an M2.2 event.

As noted in the introduction, one strategy to deal with the incompleteness is to fit the standard ETAS model only in time intervals, where completeness can be assumed according to the empirical relation. However, using this strategy would reduce and distort the available information in the example case. Removing all incomplete time intervals following $m \geq 4$ events according to Eq. (12) leads to a division of the time interval into 15 periods with approximately 80% of the total catalog events. However, 7% of the earthquakes are still missed in these expected complete periods. These numbers actually depend on the assumed empirical relation (here, Eq. 12), which is not universal, likely depending on the seismic network and the detection approach. Thus, ideally, the incompleteness relation should be first estimated for the specific data, which further complicates the approach. These numbers and facts highlight the drawbacks of the mentioned approach and favor the proposed ETASI application.

For the same example, panels Fig. 2(b)-(c) show the ETASI results for the parameter estimations. In each case, the difference of the Likelihood-value to its maximum, $\mathcal{LL}_{max} - \mathcal{LL}$, was calculated varying two parameters, while the other parameters were fixed to the actual ETAS parameters: α & K in (b), c & p in (c), and c & T_b in (d). In all cases, the maximum likelihood estimations are close to the true values marked by crosses. In particular, the difference between $\mathcal{LL}_{max}$ and the likelihood value for the true parameters is so small (less than five) that the model with fixed true parameters would be favored over the estimated maximum likelihood parameters based on the Bayesian information criterion (BIC) considering the two free parameters.

In the following, all model parameters are simultaneously estimated to test the ETASI approach for real applications. For that purpose, the $\mathcal{LL}$ in Eq. (10) is maximized considering the entire parameter space $(\mu, K, \alpha, c, p, b, T_b)$ for the given synthetic catalog. Then, the same procedure was repeated for 100 different synthetic catalogs, each consisting of another random ETAS simulation with subsequent removal of non-recordable events using the parameters mentioned above. Boxplots represent the resulting parameter estimations in Fig. 3. For each parameter, the box extends from the 25% to the 75% quantile of the estimated parameters. The horizontal line marks the median, while the bar indicates the full range of the estimated values. These estimations are compared to (i) the corresponding values resulting from applying the standard ETAS model (Eq. 8) and (ii) the true values. In addition, the fit quality is compared on the right panel of Fig. 3 using the corrected information gain per earthquake (IGPEc), which accounts for the additional parameter of the ETASI model. The IGPEc-value is determined by the difference (ΔAIC) of the corrected Akaike information criterion (AICc) between the ETASI and the ETAS model, normalized by twice of the event number (Rhoades et al., 2014, Eq. 8). The IGPEc values are all positive and scatter around 0.08, indicating a better fit of the ETASI model.

Using the standard ETAS model, all parameter estimations are found to be biased. In particular, the c-value is significantly and systematically overestimated with large uncertainties, while the overestimation of the p-value is moderate. Note that c and p estimations are known to be positively correlated, meaning that the overestimation of one of both parameters also leads to an overestimation of the other (Holschneider et al., 2012). Furthermore, the productivity parameters are also strongly biased, with a considerable overestimation of K and a significant underestimation of α. Note that the range of estimated α-value from 0.5 to 0.85 covers most of the ETAS-based estimations for real, likely incomplete catalogs, while other methods indicate values close to one (Hainzl and Marsan, 2008). Finally, the b-value is also significantly underestimated, with most estimations lying between 0.8 and 0.9. This effect of short-term incompleteness on the b-value estimation has been already recognized before (Kagan, 2004; Hainzl, 2016a).

Utilizing the ETASI approach, the parameter estimations are significantly better. The results indicate that the background rate μ, as well as the aftershock productivity parameters K and α, can be well estimated. The same holds for the Gutenberg-Richter b-value with estimations scattering around one. The Omori parameters c and p are slightly overestimated, such as the blind time T_b. The reason for this bias is likely related to broken links due to the removal of undetected earthquakes, leading to wrong associations of events. While the range of the estimated p and T_b values include the true values, the estimated c-values are in all cases larger than the true one but still significantly better than the c-estimates of the standard model.

A similar analysis was repeated for $c = 1$ s and $c = 0.1$ d. In both cases, the parameter K was adjusted to keep the same branching ratio of 0.8 (see Supplementary Material Fig. S1 and S2). In the case of the tiny c-value, more events remain undetected compared to the case analyzed above. Vice versa, the rate-dependent incompleteness plays a less significant role in the case of the large c-value. However, in both cases, the ETASI approach is also found to provide reasonable estimations of the actual ETAS parameters.

Earthquake sequences in California

After the successful test for synthetic catalogs, the ETASI model is now applied to real catalogs where the ETAS model will only approximate the real dynamics, and the true seismicity parameters are not known. In particular, ETAS parameters are estimated for the aftershock sequences of the six largest mainshocks that occurred in the last decades in California.

Data

The California data were downloaded from the Southern California Earthquake Data Center (SCEDC) and consist of 699,174 earthquakes recorded between January 1, 1981, and December 31, 2019 (see *Data and Resources*). A magnitude cutoff of $M_c = 2.05$ is used to avoid the general incompleteness of $m < 2$ events (Hutton et al., 2010). The special value of 2.05 instead of 2.0 is used because, although magnitudes are given to two decimal places, significant clustering at single-digit values indicates relics of 0.1-magnitude binning. Thus, a cutoff value of 2.0 would likely include events in the magnitude range between 1.95 and 2.0. The finally analyzed catalog consists of 118,926 earthquakes with magnitude $m \geq 2.05$.

At first, the six largest earthquakes, so-called mainshocks, were selected, which occurred within the box defined by $[32.0°\mathrm{N}, 36.5°\mathrm{N}]$ and $[-121.0°\mathrm{W}, -115.0°\mathrm{W}]$. For each of these mainshocks, the target space-time volume is defined by (i) a disk A centered at the mainshock epicenter with a radius of 100 km and (ii) a time interval of $T = [-10, 100]$ days relative to the mainshock time. All $m \geq 2.05$ events inside this volume are the target events for the ETASI fit.

As discussed at the beginning of Section *ETAS model for rate-dependent incompleteness (ETASI)*, detailed modeling of the spatial interactions is here avoided because it can lead to biased ETAS-estimations (Hainzl et al., 2008). Nevertheless, the spatial triggering can be considered to some extend by integration of Eq. (1) over A. In this way, the model considers that parts of the aftershocks are expected to be triggered outside of A as well as earthquakes that occurred outside of A might have triggered aftershocks within A. In particular, the integration leads to an replacement of Eq. (6) by

$$R_0(t) = \mu + \sum_{i:t_i<t} \kappa_i \, K \, 10^{\alpha(m_i - M_c)} \, (c + t - t_i)^{-p} \quad \text{with} \quad \kappa_i = \int_A \xi(m_i, |\vec{x} - \vec{x}_i|) \, d\vec{x} \qquad (13)$$

with κ_i being the fraction of aftershocks, which is expected to be triggered inside A (Zakharova et al., 2017). Here I used the empirical, magnitude-dependent probability density distribution derived for California seismicity consisting of three different regimes with transitions at the scale of the rupture length and the thickness of the crust (Moradpour et al., 2014, Eq. 7).

This approach not only considers that some aftershocks are triggered outside of A but also allows to include the effects of large events occurring outside this space-time volume. In particular, the sum of Eq. 13 includes all events in the target region A and target time interval. However, it also includes events outside the space-time volume, which are estimated to trigger more than 0.01 events in the total target volume AxT. In this way, finite-size effects are avoided.

The spatial and temporal distributions of the selected six mainshock-aftershock sequences are shown in Fig. 4, and the mainshock source information and the number of target and total events are summarized in Tab. 1. The earliest case is that of the 1987 Superstition Hill pair of earthquakes in the Salton Trough with magnitudes 6.2 and 6.6 separated only by approximately 12 hours. The following sequence is related to the largest mainshock, the well-known M7.3 1992 Landers earthquake, which also triggered the most extensive aftershock sequence. In 1994, the M6.7 Northridge event occurred on a blind thrust fault in the San Fernando Valley region. The selected aftershocks are almost isotropically clustered in this case, while linearly elongated distributions are observed in all other cases. In 1999, the M7.1 Hector Mine earthquake occurred in the Mojave Desert and triggered the third largest aftershock activity. An even more intensive sequence was triggered by the 2010 M7.2 Baja California mainshock, which occurred just south of California's border in Mexico. Finally, the Ridgecrest sequence consists of three major events with magnitudes of 6.4, 5.4, and 7.1, which occurred in July 2019 within 34 hours. The Ridgecrest mainshocks occurred on two perpendicular faults, an SW-NE and an NW-SE-oriented fault.

Results

Tab. 2 summarizes the parameter estimations resulting from the standard ETAS and the ETASI model (a visualization of the results is provided in the Supplementary Material Fig. S3). Besides the parameters, the table also provides the maximum likelihood values $\mathcal{LL}$ for both models, which is obtained in the case of the standard ETAS model by maximizing Eq. (8), while it is related to the maximization of Eq. (10) in the case of the ETASI model. Because the ETASI model includes an additional fitting parameter, the $\mathcal{LL}$-values cannot be directly compared. The model with more degrees of freedom is generally expected to fit better. Therefore, the value of the corrected information gain per earthquake (IGPEc) is also provided (as done for the synthetic sequences) to account for the additional parameter. A positive IGPEc-value between 0.06 and 0.11 is obtained for all six cases. The corresponding ΔAIC-values range between 442.2 and 1702.1 and $1 - \exp(-\Delta\text{AIC}/2)$ can be interpreted as the relative probability that the model with minimum AIC (here the ETASI model) minimizes the information loss (Burnham and Anderson, 2002). Thus, the ETASI model fits significantly better than the standard ETAS model.

The estimated parameters also differ significantly. Two observations are most remarkable: Firstly, the α-value increases systematically applying the ETASI model. While the ETAS model obtains low values in the range between 0.36 (Landers) and 0.66 (Ridgecrest), the estimations scatter around one in the case of the ETASI model with values between 0.88 (Landers) and 1.18 (Ridgecrest). A similar trend is observed for the b-value: The maximum likelihood estimation yields $b \in [0.79, 1.10]$ for ETAS and $b \in [0.94, 1.39]$ for ETASI. Both observations are in agreement with the results for the synthetic sequences in Section *Synthetic simulations*. For the remaining parameters, the difference between the two model estimations is not systematic, with positive and negative changes.

A visual comparison of the ETAS and ETASI model fits is shown in Fig. 5, left column. The semi-logarithmic plots show the observed earthquake magnitudes and rates as a function of the time after the mainshocks. Similar to the case of the analyzed incomplete synthetic catalogs, aftershocks with small magnitudes were missed directly after the mainshock. This deficiency is compared to the empirical completeness relation (Eq. 12) of Helmstetter et al. (2006), represented by the black dashed lines. The empirical relation is found to fit well for the four sequences before 2000 but significantly overestimates the completeness magnitudes for the latest two sequences, the 2010 Baja California and the 2019 Ridgecrest sequence. The quality of the rate fits of the ETAS and ETASI model are difficult to distinguish visually. Both fit the observed, incompletely recorded rates very well. However, the ETASI also provides the estimated true rate of $m \geq 2.05$ events, indicated in the same plots by the dashed curve. Shortly after the mainshock, these estimated true rates are found to be by a factor between 10 and 100 larger than the detected rates.

Furthermore, the ETASI model predicts a time-dependence of the frequency-magnitude distribution of the catalog events, while the standard ETAS approach implicitly assumes a constant distribution. To test whether the ETASI model fits the observation, I calculated the b-value of the observed events in time bins by the Aki-estimator (Aki, 1965, Eq. 9), which is solely dependent on the mean magnitude. I notably estimated the b-values in non-overlapping time windows consisting of $M = 100$ events with $m \geq 2.05$. The results for the empirical data are shown as black crosses in the right panels of Fig. 5, where the width and height of the crosses refer to the time interval and plus/minus one standard deviation, $b/\sqrt{M}$, of the Aki-estimator, respectively. A similar trend is observed in all cases. The estimated b-value is less than 0.5 directly after the mainshock and then continuously increases until it converges to a stable value around one. The limit value is well fitted by the estimated

b-value of the ETASI model (dashed horizontal line), while it is significantly underestimated by the standard ETAS approach (gray horizontal line). The time until convergence varied between approximately one day (Ridgecrest) and one month (Landers). The convergence phase can be compared to the forecasts of the ETASI model, whose probability density magnitude distribution (Eq. 11) is defined by the estimated true b value (Tab. 2) and the true rate $R_0(t)$ (dashed curve in the left panels of Fig. 5), which is known at all times. Thus I calculated the mean value of Eq. (11) at the times of all aftershocks and determined the related b-value by Eq. (9). The results are shown by thin solid curves in the right panels of Fig. 5. The ETASI forecasts fit very well the observed time-dependence of the empirical b-values.

Discussion

The ETASI model builds on the assumption that the short-time incompleteness is related to a blind time T_b of the detection algorithm. In this case, the detection probability for earthquakes with a magnitude m can be determined by the Poissonian probability that no larger than m event occurred within T_b before the event. An effective blind time is expected to be present in almost every detection algorithm, while its actual value will depend on the particular algorithm. For example, a classical short-term-average to long-term-average ratio (STA/LTA) picker typically uses LTA windows around 30 s (Earle and Shearer, 1994). In this period, the arrival of seismic waves related to a preceding event prevents picking a smaller magnitude event within the STA window. Because of the delayed arrival of the seismic waves and associated coda waves of preceding events, the effective blind time is even larger than the LTA window. The time between the earthquake rupture (catalog time) and a sufficient attenuation of the coda wave is of the order of one minute for local events (Wang and Shearer, 2017). Thus, for an STA/LTA-picker, the blind time is expected to be of the order of 100 s. More sophisticated methods like template-matching detection techniques might lead to a significantly shorter blind time because full waveform information is used (Ross et al., 2019). However, the approach only works well if the waveforms of subsequent events do not overlap in time, which again introduces an effective blind time of the algorithm.

For simplicity, a magnitude-independent T_b-value is assumed in the ETASI approach. The short source durations justify this simplification. Recorded waves are the result of a convolution of the crustal Green's functions with the source function. Only the latter is magnitude-dependent. However, the earthquake source durations are usually less than a few seconds for $m < 5$ events. Thus, for the vast majority of the events, the source times are much less than the travel times of the induced waves to the seismic stations, justifying the use of a constant T_b-value.

In reality, other reasons than an algorithm's blind time might lead to short-term excursions of the completeness magnitude above the general completeness level M_c. One reason might be the short-term failures of seismic stations in the network due to power outages or other problems. Another reason could be that the completeness level changed because the operators focused their hand-picking of the earthquakes' onsets in particular periods. However, the latter is less relevant for modern catalogs because recorded waveforms are nowadays processed continuously with the same algorithms. Thus the ETASI approach is assumed to be best suited for most recent catalogs processed by automatized algorithms on continuous waveforms.

For our analyzed sequences in California, the estimated values of the blind time T_b significantly decrease with the date (Tab. 2). While T_b is in the range between 140 and 200 s before 2000, it is only 27 s for the last Ridgecrest sequence in 2019, as visualized in Fig. 6b. This observation indicates an improving detection algorithm of the Southern California Earthquake Data Center (SCEDC) over time.

The ETASI model allows addressing the c-value in more detail. The c-estimations based on catalog data are typically in the order of hours to days depending on the mainshock and cutoff magnitude (Utsu et al., 1995; Hainzl, 2016b). However, the catalog's short-term incompleteness affects the c-estimations significantly. For case examples in California and Japan, sophisticated reprocessing of the recorded seismograms revealed many additional events missed by routine detection procedures, reducing c to values in the order of minutes (Kagan, 2004; Kagan and Houston, 2005; Peng et al., 2006, 2007; Enescu et al., 2007). These systematic studies indicate that c-values estimated, e.g., by the standard ETAS approach, are at least partially related to the catalog's incompleteness rather than the aftershock triggering mechanism. However, in principle, the ETASI model allows estimating the true c-value related to earthquake triggering by accounting for the catalog's short-term incompleteness. The estimated value range between 2 minutes for Ridgecrest and 20 hours for Landers. Most values are significantly smaller than the estimations of the ETAS model, except Landers and Northridge. Notably, the high value for the Landers sequence is questionable. To analyze the uncertainties of the c-value estimates, I recalculated the maximum likelihood value optimizing all parameters besides the c-value, which was varied systematically between 10 and 10^5 s. The resulting IGPEc values are shown in Fig. 6a for all six sequences. The figure shows that for all analyzed c-values and sequences, the ETASI fit (solid line) is superior to the best fit of the ETAS model (horizontal dashed line). Furthermore, the curves have a broad maximum indicating large uncertainties of the c-estimations. In particular, by defining the uncertainties according to an IPGEc-margin of 0.01 (gray horizontal bar), the uncertainties of all estimations almost overlap: For Ridgecrest and Superstition Hill, only upper bounds of 15 min and 1.5 h are defined but no lower limit. In contrast, c ranges between 30 s and 4 h for Baja California and between 6 min and 8 h for Northridge. Finally, only a lower limit of approximately 30 min can be defined for both Hector Mine and Landers. However, the synthetic tests in Section *Synthetic simulations* indicate that all c-values might be slightly overestimated. Furthermore, the estimated uncertainty does not yet account for violations of the model assumptions, such as additional sources of incompleteness mentioned above.

Thus the true uncertainties will be even larger, indicating that a physical interpretation of the estimated c-values remains a difficult task.

The performed synthetic tests and application to California sequences show that ignoring short-term incompleteness of earthquake catalogs leads to significantly biased parameters, which might strongly affect forecasts of the ETAS model. The underestimated α-value leads to an underestimation of the number of direct aftershocks triggered by large earthquakes. In contrast, the underestimated b-value overestimates the magnitudes of these events, leading to stronger secondary triggering. The impact of the combined effect depends on the specific parameters and the target quantity. A systematic analysis of the effect on forecasts is out of the scope of this paper. However, as an example, I calculated the foreshock probability of a magnitude 6.0 event, i.e., the probability that one of the aftershocks of an M6 event is larger than 6.0. For this purpose, I performed 1000 synthetic ETAS-simulations starting with an M6 event using the ETAS and ETASI parameters estimated for Ridgecrest (Tab. 2). The resulting foreshock probability is found to be 93%, given the parameters estimated by the standard ETAS approach. If a standard b-value of 1.0 is used instead of the estimated value of 0.79, the estimated probability drops to 3%. In contrast, using the parameters estimated with ETASI, the foreshock probability is estimated to be 9%, demonstrating the strong impact of considering short-term catalog incompleteness.

In some applications, the use of a simple Omori-Utsu decay might be sufficient to fit the aftershock activity. In this case, the same maximum likelihood approach (Eq. 10) can be used, where $R(t)$ and $f(m,t)$ are calculated by Eq. (3) and (11) with $R_0(t) = K(c+t)^{-p}$ and $N_0(t) = K[(c+t)^{1-p} - (c+t-T_b)^{1-p}]/(1-p)$ for $p \neq 1$, or $N_0(t) = K[\log(c+t) - \log(c+t-T_b)]$ for $p = 1$.

In this paper, the time-dependent version of the ETAS model is considered because of its simplicity and the mentioned potential problems using isotropic spatial kernels. However, an extension to a full space-time version is straightforward. Instead of Eq. (10), one simply has to maximize

$$\mathcal{LL} = \sum_{i=1}^{N} \ln\left[R(t_i, \vec{x}_i) f(m_i, t_i)\right] - \int_{T_1}^{T_2} \int_{A} R(t, \vec{x}) \, dt \, d\vec{x}$$

with $R(t, \vec{x})$ being determined by the first part of Eq. (3), i.e.,

$$R(t, \vec{x}) = R_0(t, \vec{x}) \, \frac{1 - e^{-N_0(t)}}{N_0(t)} \ , \tag{14}$$

where $R_0(t, \vec{x})$ is given by Eq. (1). The detection probability is dependent on the total activity in the analyzed area within the blind time. Thus, $N_0(t)$ used for the calculation of

$R(t, \vec{x})$ (Eq. 14) and $f(m_i, t_i)$ (Eq. 11) is given in this case by

$$N_0(t) = \int_{t-T_b}^{t} \int_A R_0(t, \vec{x})\ dt\, d\vec{x} \quad \approx \ T_b \int_A R_0(t, \vec{x})\, d\vec{x}\ ,$$

where the approximation is possible due to the short duration of T_b.

Conclusion

The ETAS model is presently maybe the most powerful statistical seismicity model, reproducing the general characteristics of spatiotemporal earthquake clustering. However, its application and forecast ability can be hampered by biased parameter estimations related to catalog deficiencies. In particular, it has been recognized that the short-term incompleteness can significantly bias the forecasts of the aftershock productivity and magnitudes (Kagan, 2004; Hainzl et al., 2013; Hainzl, 2016a). Several methods have already been introduced before to deal with this problem (Hainzl et al., 2013; Omi et al., 2013, 2014; Zhuang et al., 2017). However, the proposed ETASI-approach provides, for the first time, a closed-form maximum likelihood approach accounting for the short-time incompleteness of earthquake catalogs. The ETASI model has only one additional parameter, namely the blind time T_b representing the time after an earthquake in which subsequent events with smaller magnitude are missed by the network's detection algorithm.

The ETASI model allows estimating the real parameters relevant for seismic hazard assessment, such as the aftershock productivity and the Gutenberg-Richter b-value. The performed synthetic tests show that both are largely underestimated if short-time incompleteness is ignored, while the ETASI model can retrieve the true values. The application to major mainshock-aftershock sequences in California also leads to superior fits of the ETASI model with similar parameter trends, where the resolved productivity parameter α is found to be close to one. The results indicate that large-magnitude events have a significantly larger trigger potential than previously thought.

Data and Resources

The California earthquake catalog has been downloaded from the Southern California Earthquake Data Center (SCEDC, https://scedc.caltech.edu/research-tools/alt-2011-dd-hauksson-yang-shearer.html) on October 8, 2020. The Supplemental Material includes two figures similar to Fig. 3 but for a smaller and larger c-value, respectively. Furthermore, it includes a third figure illustrating the estimated parameters for California's sequences provided in Tab. 2.

Acknowledgments

I want to thank Leila Mizrahi and her colleagues for sharing their work related to an iterative EM-algorithm for ETAS accounting for short-term incompleteness (https://arxiv.org/abs/2105.00888). I am also grateful to Kaoru Sawazaki and an anonymous reviewer for their helpful comments and suggestions. This study was supported by the DFG Collaborative Research Centre 1294 (Data Assimilation - The seamless integration of data and models, project B04).

References

Aki, K. (1965). Maximum likelihood estimate of b in the formula $\log N = a - bM$ and its confidence limits, *Bull. Earthquake Res. Inst.*, **43**, 237–239.

Burnham, K. P., and D. R. Anderson (2002). Model selection and multimodel inference: A practical information-theoretic approach, Springer-Verlag, 2nd ed., paragraph 6.4.5.

de Arcangelis, L., C. Godano, and E. Lippiello (2018). The overlap of aftershock coda waves and short-term postseismic forecasting, *J. Geophys. Res.* **123**, 5661–5674.

Earle, P. S., and P. M. Shearer (1994). Characterization of global seismograms using an automatic-picking algorithm, *Bull. Seismol. Soc. Am.* **84**, 366–376.

Enescu, B., J. Mori, and M. Miyazawa (2007). Quantifying early aftershock activity of the 2004 mid-Niigata Prefecture earthquake ($\mathrm{M_w}$6.6), *J. Geophys. Res.* **112**, B04310, doi:10.1029/2006JB004629.

Felzer, K. R., T. W. Becker, R. E. Abercrombie, G. Ekstrom, and J. R. Rice (2002). Triggering of the 1999 M_w 7.1 Hector Mine earthquake by aftershocks of the 1992 M_w 7.3 Landers earthquake, *J. Geophys. Res.* , **107**, 2190, doi:10.1029/2001JB000911.

Hainzl, S. (2016a). Rate-dependent incompleteness of earthquake catalogs, *Seismol. Res. Lett.* **87**, 337–344.

Hainzl, S. (2016b). Apparent triggering function of aftershocks resulting from rate-dependent incompleteness of earthquake catalogs, *J. Geophys. Res.* **121**, 6499–6509.

Hainzl, S., and D. Marsan (2008). Dependence of the Omori-Utsu law parameters on main shock magnitude: Observations and modeling, *J. Geophys. Res.* **113**, B10309, doi:10.1029/2007JB005492.

Hainzl, S., A. Christophersen, and B. Enescu (2008). Impact of earthquake rupture extensions on parameter estimations of point-process models, *Bull. Seismol. Soc. Am.* **98**, 2066–2072.

Hainzl, S., O. Zakharova, and D. Marsan (2013). Impact of aseismic transients on the estimation of aftershock productivity parameters, *Bull. Seismol. Soc. Am.* **103**, 1723–1732, doi: 10.1785/0120120247.

Hauksson, E., P. M. Shearer, and W. Yang (2012). Waveform Relocated Earthquake Catalog for Southern California (1981 to June 2011). *Bull. Seismol. Soc. Am.* **102**, 2239–2244.

Helmstetter, A., and D. Sornette (2002). Subcritical and supercritical regimes in epidemic models of earthquake aftershocks, *J. Geophys. Res.* **107**, 2237, doi:10.1029/2001JB001580.

Helmstetter, A., Y. Y. Kagan, and D. D. Jackson (2006). Comparison of short-term and time-independent earthquake forecast models for southern California, *Bull. Seismol. Soc. Am.* **96**(1), 90–106.

Holschneider, M., C. Narteau, P. Shebalin, Z. Peng, and D. Schorlemmer (2012). Bayesian analysis of the modified Omori law, *J. Geophys. Res.* **117**, B06317, doi:10.1029/2011JB009054.

Hutton, K., J. Woessner, and E. Hauksson (2010). Earthquake monitoring in southern California for seventy-seven years (1932–2008), *Bull. Seismol. Soc. Am.* **100**, 423–446.

Kagan, Y. Y. (2004). Short-term properties of earthquake catalogs and models of earthquake source, *Bull. Seismol. Soc. Am.* **94**(4), 1207–1228.

Kagan, Y. Y., and H. Houston (2005). Relation between mainshock rupture process and Omori's law for aftershock moment release rate, *Geophys. J. Int.* **163**, 1039–1048.

Lippiello, E., A. Cirillo, G. Godano, E. Papadimitriou, E., and V. Karakostas (2016). Real-time forecast of aftershocks from a single seismic station signal, *Geophys. Res. Lett.* **43**, 6252–6258.

Marsan, D., and Z. E. Ross (2021). Inverse migration of seismicity quiescence during the 2019 Ridgecrest sequence, *J. Geophys. Res.* **126**, e2020JB020329, doi:10.1029/2020JB020329.

Moradpour, J., S. Hainzl, and J. Davidsen (2014). Nontrivial decay of aftershock density with distance in Southern California, *J. Geophys. Res.* **119**, 5518–5535.

Ogata, Y. (1988). Statistical models of point occurrences and residual analysis for point processes, *J. Am. Stat. Assoc.*, **83** 9-27.

Ogata, Y. (1998). Space-time point-process models for earthquake occurrences, *Ann. Inst. Statist. Math.* **50**, 379-402.

Omi, T., Y. Ogata, Y. Hirata, and K. Aihara (2013). Forecasting large aftershocks within one day after the main shock, *Sci. Rep.* **3**, 2218, doi:10.1038/srep02218.

Omi, T., Y. Ogata, Y. Hirata, and K. Aihara (2014). Estimating the ETAS model from an early aftershock sequence, *Geophys. Res. Lett.* **41**, 850–857, doi:10.1002/2013GL058958.

Peng, Z. G., J. E. Vidale, and H. Houston (2006). Anomalous early aftershock decay rate of the 2004 Mw6.0 Parkfield, California, earthquake, *Geophys. Res. Lett.* **33**, L17307, doi:10.1029/2006GL026744.

Peng, Z. G., J. E. Vidale, M. Ishii, and A. Helmstetter (2007). Seismicity rate immediately before and after main shock rupture from high-frequency waveforms in Japan, *J. Geophys. Res.* **112**, B03306, doi:10.1029/2006JB004386.

Rhoades, D. A., M. C. Gerstenberger, A. Christophersen, J. D. Zechar, D. Schorlemmer, M. J. Werner, and T. H. Jordan (2014). Regional earthquake likelihood models II: Information gains of multiplicative hybrids, *Bull. Seismol. Soc. Am.* **104**, 3072–3083.

Ross, Z. E., D. T. Trugman, E. Hauksson, and P. M. Shearer (2019). Searching for hidden earthquakes in Southern California, Science **364**, 767–771.

Seif, S., A. Mignan, J. D. Zechar, M. J. Werner, and S. Wiemer (2017). Estimating ETAS: The effects of truncation, missing data, and model assumptions, *J. Geophys. Res.* **122**, 449–469.

Utsu, T., Y. Ogata, and R. S. Matsu'ura (1995). The centenary of the Omori formula for a decay of aftershock activity, *J. Phys. Earth*, **43** 1–33.

Wang, W., and P. M. Shearer (2017). Using direct and coda wave envelopes to resolve the scattering and intrinsic attenuation structure of Southern California, *J. Geophys. Res.* **122**, 7236–7251.

Zakharova, O., S. Hainzl, D. Lange, and B. Enescu (2017). Spatial variations of aftershock parameters and their relation to geodetic slip models for the 2010 Mw8.8 Maule and the 2011 Mw9.0 Tohoku-oki earthquakes, *Pure Appl. Geophys.* **174**, 77–102.

Zhuang, J., and S. Touati (2015). Stochastic simulation of earthquake catalogs, *Community Online Resource for Statistical Seismicity Analysis*, doi:10.5078/corssa-43806322. Available at http://www.corssa.org.

Zhuang, J., Y. Ogata, and T. Wang (2017). Data completeness of the Kumamoto earthquake sequence in the JMA catalog and its influence on the estimation of the ETAS parameters, *Earth. Planets and Space* **69**, 36, doi:10.1186/s40623-017-0614-6.

Address

Sebastian Hainzl, Helmholtz-Zentrum Potsdam: Deutsches GeoForschungsZentrum GFZ, Telegrafenberg, 14473 Potsdam, Germany

Table 1: Information concerning the six selected mainshock-aftershock sequences in California and Baja California. The target area A is defined by a disk centered at the mainshock epicenter with a radius of 100 km, and the fitted period extends from -10 to 100 days relative to the mainshock occurrence. The second last column provides the number N of target events within this volume, while the number N_{tot} in the last column also includes the events outside of AxT used in Eq. (13).

Name	Year	Magnitude	Epicenter	$N(m \geq 2.05,\ A\mathrm{x}T)$	N_{tot}
Superstition Hill	1987	6.6	33.01°N, -115.83°W	2398	2526
Landers	1992	7.3	34.20°N, -116.44°W	9295	10157
Northridge	1994	6.7	34.23°N, -118.54°W	2166	2226
Hector Mine	1999	7.1	34.60°N, -116.27°W	3988	4164
Baja California	2010	7.2	32.30°N, -115.29°W	7245	7485
Ridgecrest	2019	7.1	35.77°N, -117.60°W	5285	5343

Table 2: Estimated parameters of the selected mainshock-aftershock sequences in California resulting from maximizing Eq. (8) according to the standard ETAS approach or Eq. (10) using the ETASI model. The column $\mathcal{LL}$ refers to the maximum likelihood value, and IGPEc is the corrected information gain per earthquake relative to the ETAS model (Rhoades et al., 2014). The standard errors of the parameters are determined by the inverse of the Hessian matrix of the log-likelihood function.

Sequence	model	μ [1/day]	K	α	c [min]	p	b	T_b [s]	$\mathcal{LL}$	IGPEc
Superstition Hill	ETAS	0.9 ± 0.2	0.068 ± 0.009	0.55 ± 0.02	105 ± 47	1.37 ± 0.02	1.10 ± 0.02		7903	0
	ETASI	1.5 ± 0.1	0.006 ± 0.010	1.02 ± 0.01	10 ± 22	1.21 ± 0.01	1.39 ± 0.01	141 ± 79	8176	0.11
Landers	ETAS	0.2 ± 0.7	0.093 ± 0.009	0.36 ± 0.02	93 ± 40	1.31 ± 0.02	0.93 ± 0.01		34801	0
	ETASI	1.8 ± 0.3	0.101 ± 0.041	0.88 ± 0.01	1197 ± 117	1.60 ± 0.03	1.22 ± 0.01	182 ± 44	35653	0.09
Northridge	ETAS	0.2 ± 0.2	0.049 ± 0.008	0.46 ± 0.02	35 ± 48	1.26 ± 0.02	0.80 ± 0.02		6677	0
	ETASI	0.4 ± 0.1	0.004 ± 0.012	1.06 ± 0.02	77 ± 49	1.32 ± 0.01	1.02 ± 0.01	156 ± 87	6899	0.10
Hector Mine	ETAS	0.8 ± 0.2	0.118 ± 0.025	0.64 ± 0.04	840 ± 261	1.43 ± 0.02	0.96 ± 0.02		13072	0
	ETASI	1.3 ± 0.2	0.017 ± 0.022	0.96 ± 0.02	336 ± 73	1.33 ± 0.02	1.23 ± 0.01	199 ± 77	13503	0.11
Baja California	ETAS	0.4 ± 0.3	0.054 ± 0.005	0.46 ± 0.01	35 ± 21	1.26 ± 0.01	0.81 ± 0.01		26212	0
	ETASI	0.1 ± 0.4	0.008 ± 0.001	0.97 ± 0.00	25 ± 18	1.09 ± 0.01	0.94 ± 0.01	77 ± 1	26618	0.06
Ridgecrest	ETAS	0.1 ± 0.2	0.029 ± 0.005	0.66 ± 0.01	38 ± 21	1.24 ± 0.01	0.79 ± 0.01		22424	0
	ETASI	0.2 ± 0.1	7.9e-4±5.7e-4	1.18 ± 0.01	2 ± 17	1.17 ± 0.01	1.00 ± 0.01	27 ± 53	23138	0.13

Figure Captions

Fig. 1: Illustration of the theoretical relations Eq. (3) and Eq. (4) for incomplete catalogs: (a) The apparent rate R as a function of the true rate R_0 for three different blind times T_b (solid lines), where the dotted line refers to a complete recording. (b) The shape of the apparent frequency-magnitude $F(m)$ for $T_b = 60$ s and three different values of R_0. Here the dotted line refers to the true underlying Gutenberg-Richter distribution (Eq. 5) with $b = 1$.

Fig. 2: Example of the ETASI approach for an ETAS simulation with $\mu = 1.0$ d^{-1}, $\alpha = 1.0$, $c = 0.001$ d, $p = 1.2$, $b = 1$, $M_{min} = 2.0$, and $M_{max} = 7.0$, where a blind time of $T_b = 60$ s was used to remove non-detectable earthquakes and create the analogs of real catalogs: (a) Event magnitudes versus time, where points and crosses indicate detected and missed events, respectively. The inset shows the same for logarithmic times relative to the mainshock, where the dashed line represents the empirical completeness function for California (Eq. 12). The small panels (b)-(d) show the contour plots of the difference of the Likelihood-value, $\mathcal{LL}_{max} - \mathcal{LL}$, as a function of two parameters, while the other parameters are fixed to the actual ETAS parameters. Crosses mark the true values.

Fig. 3: The inversion results for 100 different synthetic sequences, corresponding to the example shown in Fig. 2(a). The boxes extend from the lower to upper quartile values of the estimated parameters, with a horizontal line at the median, while the bars indicate the full range of the results. The horizontal dashed lines refer to the true parameter values. The right plot shows the corrected information gain per earthquake (IGPEc) of ETASI relative to the ETAS model.

Fig. 4: Illustration of the six selected sequences from California. For each of them, the upper panel shows the magnitude versus time plot of the sequence, while the bottom plot shows the corresponding epicenter distribution, where the central big point marks the epicenter of the corresponding mainshock, which is named in the title together with its magnitude and occurrence time.

Fig. 5: Results of the model fit to the selected sequences in California, shown in Fig. 4, where each row belongs to the mainshock named in the right plot. The left column shows the earthquake rate (with the scale on the left side) as a function of the logarithmic time after the mainshock. Here, black crosses refer to the observed rates, while lines indicate the mean rates for the optimized models: standard ETAS (bold gray) and apparent R (thin solid), respectively actual R_0 (thin dashed) rates of the ETASI model. For information, the recorded event magnitudes and the empirical completeness-relation Eq. (12) (black dashed line) are also plotted (scale on the right). In all examples, a gap of small magnitude events is visible immediately after the mainshock. In the right column, black crosses show the estimated b-values for non-overlapping bins with

100 aftershocks as a function of time. The horizontal error defines the events' time interval, and the vertical one refers to plus/minus one standard deviation of the b-value uncertainty. In the same plot, the solid curve indicates the apparent b-values related to the ETASI magnitude distribution (Eq. 11). The horizontal dashed line marks the estimated true b-value, while the dotted horizontal line indicates the estimated b-value assuming completeness all time long.

Fig. 6: (a) Dependence of the ETASI fit quality as a function of the assumed c-value, where points mark the optimal value c_0. The quality is measured by the corrected information gain per earthquake (IGPEc) relative to the optimal solution. The region with a rather insignificant loss of the fit quality (IGPEc> -0.01) is marked in gray. The horizontal dashed lines refer to the best fits of the standard ETAS model. (b) The estimated blind times as a function of the mainshock date, where the vertical bars refer to the standard errors provided in Tab. 2. Last mainshocks have a significantly smaller T_b-value, indicating an improved detection.

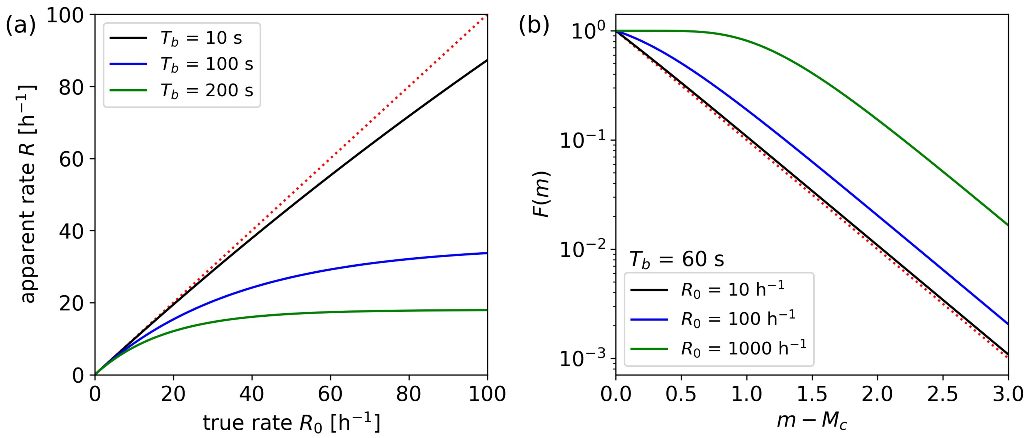

Figure 1: Illustration of the theoretical relations Eq. (3) and Eq. (4) for incomplete catalogs: (a) The apparent rate R as a function of the true rate R_0 for three different blind times T_b (solid lines), where the dotted line refers to a complete recording. (b) The shape of the apparent frequency-magnitude $F(m)$ for $T_b = 60$ s and three different values of R_0. Here the dotted line refers to the true underlying Gutenberg-Richter distribution (Eq. 5) with $b = 1$.

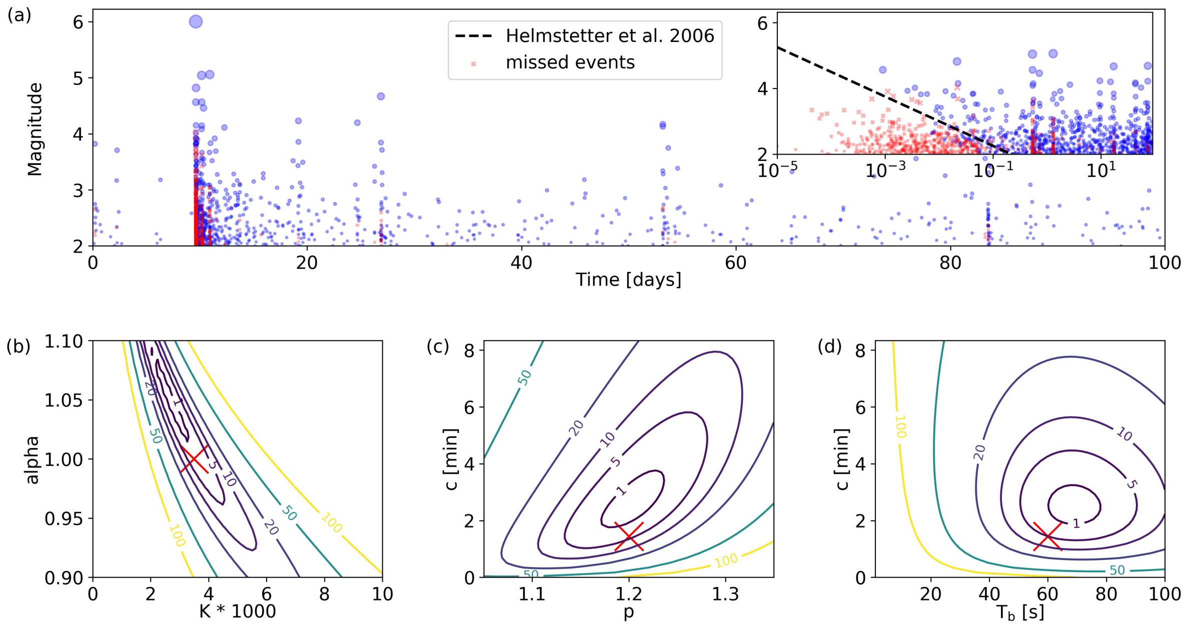

Figure 2: Example of the ETASI approach for an ETAS simulation with $\mu = 1.0$ d^{-1}, $\alpha = 1.0$, $c = 0.001$ d, $p = 1.2$, $b = 1$, $M_{min} = 2.0$, and $M_{max} = 7.0$, where a blind time of $T_b = 60$ s was used to remove non-detectable earthquakes and create the analogs of real catalogs: (a) Event magnitudes versus time, where points and crosses indicate detected and missed events, respectively. The inset shows the same for logarithmic times relative to the mainshock, where the dashed line represents the empirical completeness function for California (Eq. 12). The small panels (b)-(d) show the contour plots of the difference of the Likelihood-value, $\mathcal{LL}_{max} - \mathcal{LL}$, as a function of two parameters, while the other parameters are fixed to the actual ETAS parameters. Crosses mark the true values.

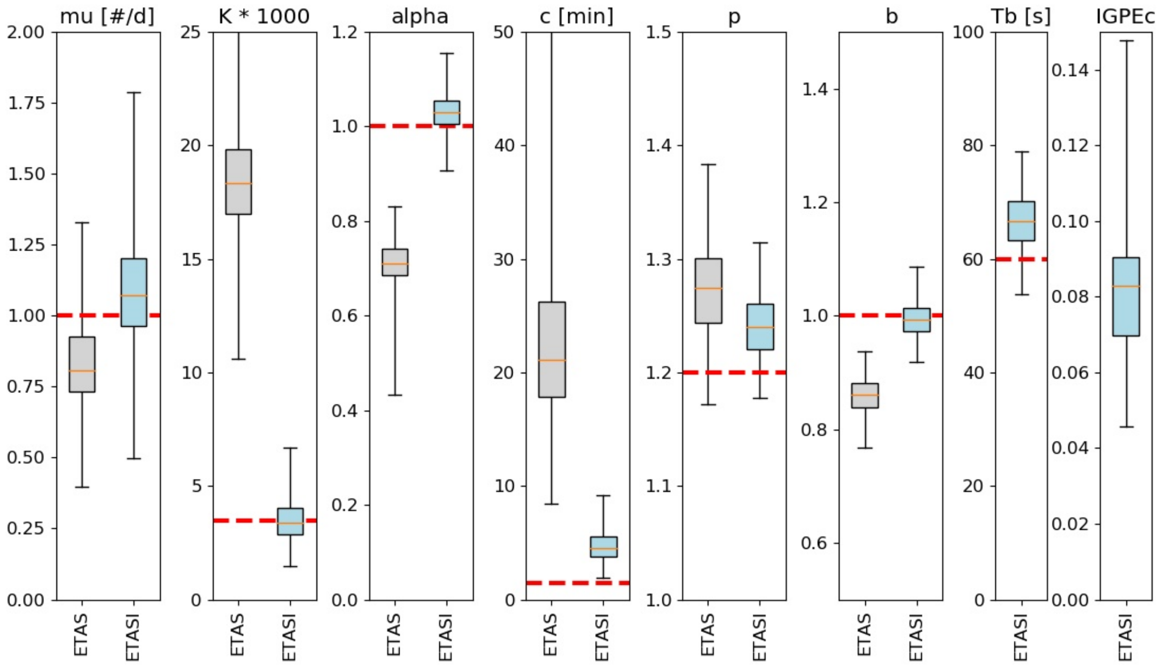

Figure 3: The inversion results for 100 different synthetic sequences, corresponding to the example shown in Fig. 2(a). The boxes extend from the lower to upper quartile values of the estimated parameters, with a horizontal line at the median, while the bars indicate the full range of the results. The horizontal dashed lines refer to the true parameter values. The right plot shows the corrected information gain per earthquake (IGPEc) of ETASI relative to the ETAS model.

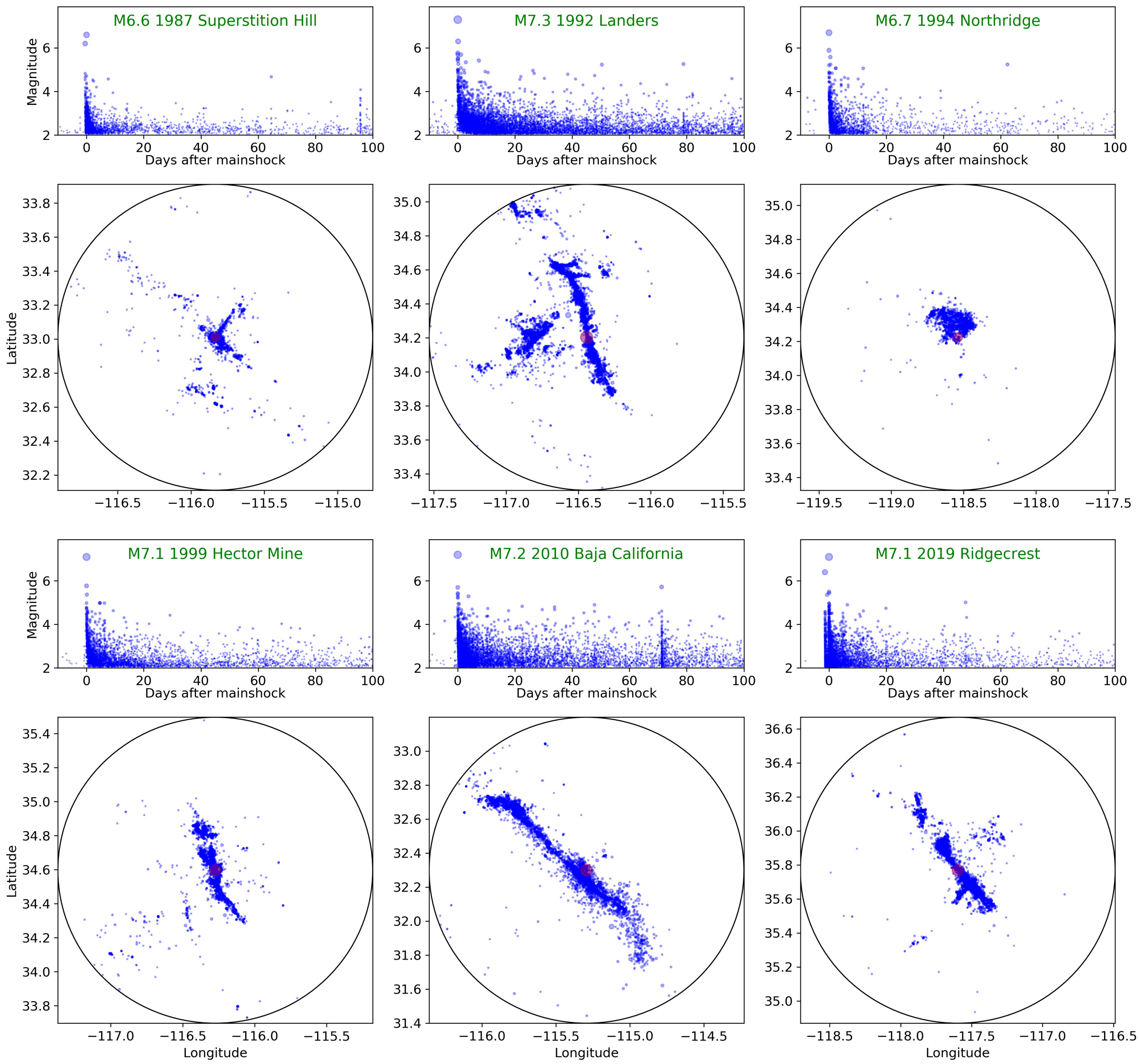

Figure 4: Illustration of the six selected sequences from California. For each of them, the upper panel shows the magnitude versus time plot of the sequence, while the bottom plot shows the corresponding epicenter distribution, where the central big point marks the epicenter of the corresponding mainshock, which is named in the title together with its magnitude and occurrence time.

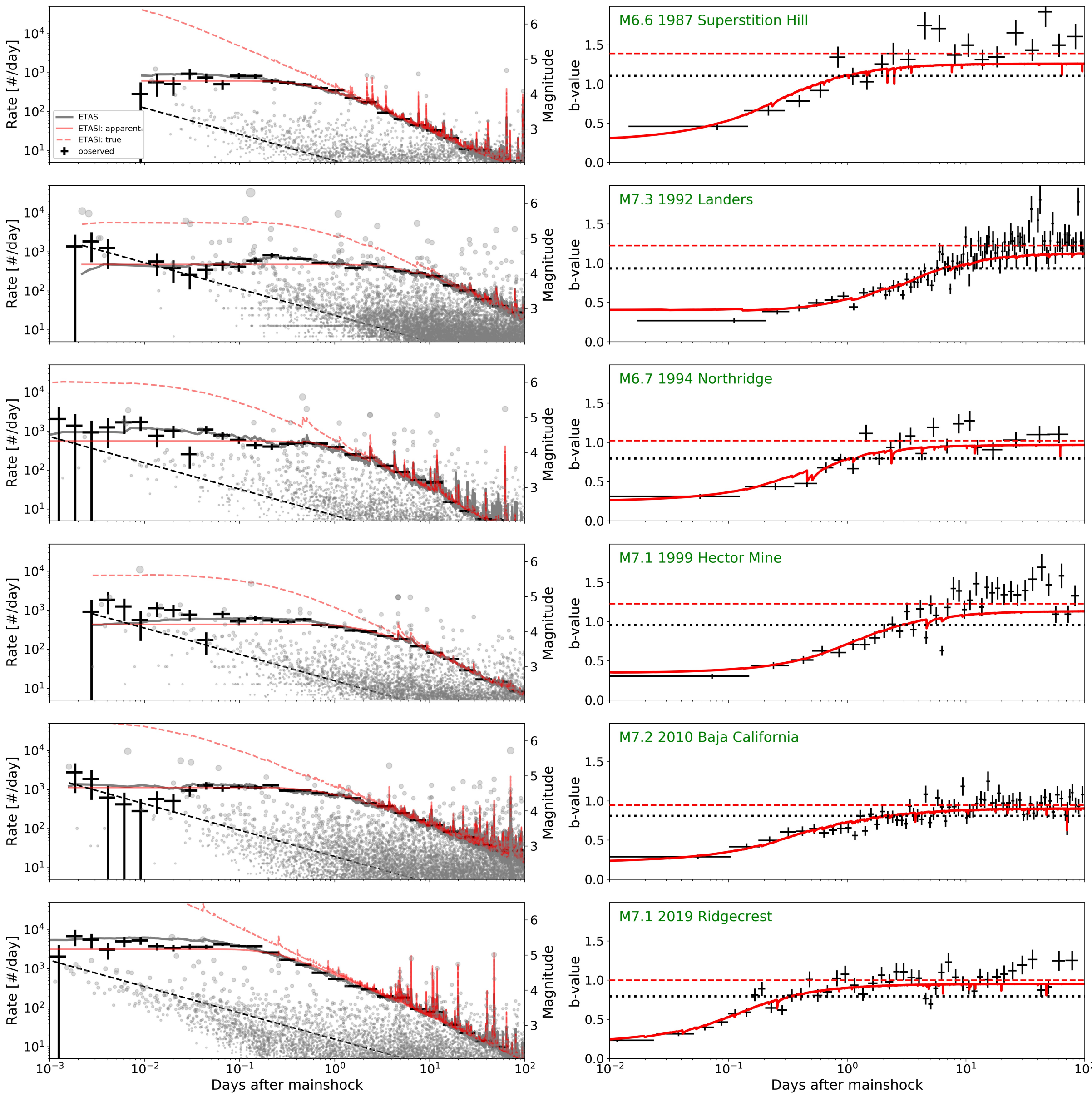

Figure 5: Results of the model fit to the selected sequences in California, shown in Fig. 4, where each row belongs to the mainshock named in the right plot. The left column shows the earthquake rate (with the scale on the left side) as a function of the logarithmic time after the mainshock. Here, black crosses refer to the observed rates, while lines indicate the mean rates for the optimized models: standard ETAS (bold gray) and apparent R (thin solid), respectively actual R_0 (thin dashed) rates of the ETASI model. For information, the recorded event magnitudes and the empirical completeness-relation Eq. (12) (black dashed line) are also plotted (scale on the right). In all examples, a gap of small magnitude events is visible immediately after the mainshock. In the right column, black crosses show the estimated b-values for non-overlapping bins with 100 aftershocks as a function of time. The horizontal error defines the events' time interval, and the vertical one refers to plus/minus one standard deviation of the b-value uncertainty. In the same plot, the solid curve indicates the apparent b-values related to the ETASI magnitude distribution (Eq. 11). The horizontal dashed line marks the estimated true b-value, while the dotted horizontal line indicates the estimated b-value assuming completeness all time long.

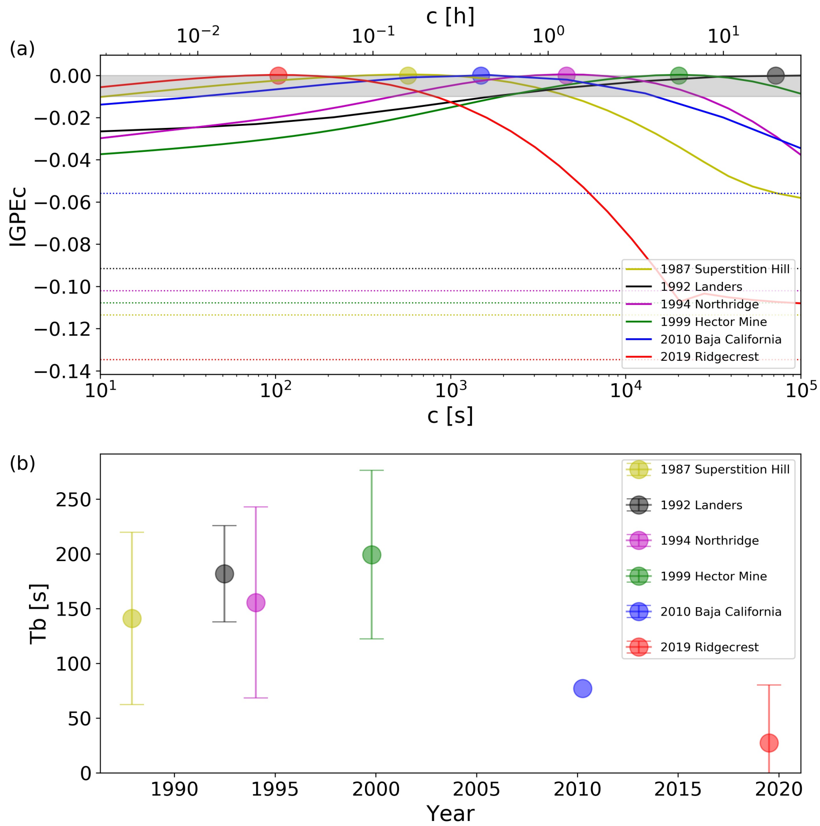

Figure 6: (a) Dependence of the ETASI fit quality as a function of the assumed c-value, where points mark the optimal value c_0. The quality is measured by the mean information gain per event, IG $= (\mathcal{LL}(c) - \mathcal{LL}(c_0))/N$. The region with a rather insignificant loss of the fit quality (IG> -0.01) is marked in gray. The horizontal dashed lines refer to the best fits of the standard ETAS model. (b) The estimated blind times as a function of the mainshock date, where the vertical bars refer to the standard errors provided in Tab. 2. Last mainshocks have a significantly smaller T_b-value, indicating an improved detection.